

## Final Response to Anonymous Referee #1

We thank Anonymous Referee #1 for the evaluation and recommendations. In the following, a point-by-point reply is given, with the Referee comments in italic. Page and line numbers in the replies refer to the marked-up version of the manuscript.

*1. page 3, between Line 20 and 25, "The intercalibration revealed offsets in the operational SEVIRI calibration of about -8%, -6% (-4% for MSG-3) and +3% in channels 1 (0.6  $\mu\text{m}$ ), 2 (0.8  $\mu\text{m}$ ), and 3 (1.6  $\mu\text{m}$ ), respectively." This statement is not clear, needs to be reworded.*

This statement was rephrased to "The inter-calibration with MODIS changed the reflectances by about -8% in channel 1 (0.6  $\mu\text{m}$ ), -6% (-4% for MSG-3) in channel 2 (0.8  $\mu\text{m}$ ), and +3% in channel 3 (1.6  $\mu\text{m}$ ) compared to the operational SEVIRI calibration provided by EUMETSAT" (page 3, lines 22-24).

*2. page 5, between Line 1 and 5, "CPP is based on look-up tables (LUTs) of top-of-atmosphere (TOA) reflectances simulated by the Doubling Adding KNMI (DAK) radiative transfer model (Stammes, 2001)." Why using DAK, any better than DISORT?*

The main reason for choosing DAK is that it has been used at KNMI since a long time for numerous applications (as clarified in page 5, lines 8-9), including for example:

- Airmass factor calculation for NO<sub>2</sub> retrieval (Boersma et al., 2004)
- Aerosol direct radiative effect over clouds (De Graaf et al., 2012)
- Absorbing Aerosol Index retrieval (Tilstra et al., 2012)

Therefore, we know very well how the model works and how it performs. In addition, because of the doubling-adding approach, DAK is very efficient for the simulation of multiple scattering cases.

Boersma, K. F., H. J. Eskes, and E. J. Brinksma: Error analysis for tropospheric NO<sub>2</sub> retrieval from space, *J. Geophys. Res.*, 109, D04311, doi:10.1029/2003JD003962, 2004.

de Graaf, M., L. G. Tilstra, P. Wang, and P. Stammes: Retrieval of the aerosol direct radiative effect over clouds from spaceborne spectrometry, *J. Geophys. Res.*, 117, D07207, doi:10.1029/2011JD017160, 2012.

Tilstra, L. G., M. de Graaf, I. Aben, and P. Stammes: In-flight degradation correction of SCIAMACHY UV reflectances and Absorbing Aerosol Index, *J. Geophys. Res.*, 117, D06209, doi:10.1029/2011JD016957, 2012.

*3. page 9, between line 25 and 30, "On the other hand, cloud fraction in the tropics is underestimated by CLAAS-2, probably due to the frequent presence of cirrus clouds in this area, which are more likely to be detected by CALIOP." For this statement, it is appropriate to cite:*

*Wenbo Sun, Gorden Videen, Seiji Kato, Bing Lin, Constantine Lukashin, and Yongxiang Hu, "A study of subvisual clouds and their radiation effect with a synergy of CERES, MODIS, CALIPSO and AIRS data," J. Geophys. Res.*, 116, doi: 10.1029/2011JD016422 (2011).

*Wenbo Sun, Bing Lin, Yongxiang Hu, Constantine Lukashin, Seiji Kato, and Zhaoyan Liu, "On the consistency of CERES longwave flux and AIRS temperature and humidity profiles," J. Geophys. Res.*, 116, D17101, doi: 10.1029/2011JD016153 (2011).

Thanks for these references: we feel the first one is sufficient and have added it to the manuscript. (page 10, line 16 and page 22, lines 16-17).

4. page 10, between line 1 and 5, *"It should be noted that the CLAAS-2 histogram extensions above 0°C for ice clouds and below -40°C for liquid clouds should be attributed to the fact that CTT in this figure comes from CALIOP. If CLAAS-2 CTT was used instead, such cases would not be allowed by the retrieval algorithm." This statement is not clear, needs to be reworded.*

This statement was rephrased to "It should be noted that the CLAAS-2 histogram extensions above 0 °C for ice clouds (red dashed line in Fig. 3) and below -42 °C for liquid clouds (red solid line in Fig. 3) should be attributed to the fact that the x-axis CTT binning in this figure comes from CALIOP. The CLAAS-2 CTT is always below 0 °C for ice clouds and above -42 °C for liquid clouds. Hence, these histogram extensions are related to CALIOP retrieving higher CTT (former case) or lower CTT (latter case) than CLAAS-2." Note that -40 °C should have been -42 °C, and this has been corrected as well. (page 10, lines 20-24).

5. page 10, between line 10 and 15, *"In contrast to binary variables like cloud mask and cloud phase, cloud top variables are continuous so that a correlation analysis can be performed.." This statement is not clear, needs to be reworded.*

This statement was rephrased to "In contrast to level 2 cloud mask and cloud phase variables, which acquire values of only 0 or 1, cloud top variables are continuous so that a correlation analysis can be performed." (page 11, lines 1-2).

6. Section 4.2 is not well expressed, need to be revised.

Section 4.2 was revised accordingly (lines 7-23 of page 11).

7. page 11, between line 9 and 17, *"For ice clouds, CLAAS-2 acquires overall lower REF, which is most probably related to the choice of ice particle habits: i.e. severely roughened monodisperse hexagonal columns for CLAAS-2 versus severely roughened aggregated columns with a gamma size distribution (Yang et al., 2013) for MODIS C6. Consistent with the results of the REF intercomparison, the agreement for LWP is better than for IWP." Are severely roughened hexagonal columns true for ice clouds? This must be checked by other particle shapes.*

In real ice clouds, a complex and variable mixture of ice particles occurs. For satellite retrievals the goal is to find a suitable simplified model that reflects the overall observed radiative properties. Knap et al. (2005) demonstrated that imperfect / roughened hexagonal columns yield adequate (and in fact better than other particles tested) simulations of total and polarized ice cloud reflectances observed by POLDER. This point is clarified in page 23, lines 8-10.

Knap, W. H., Labonnote, L. C., Brogniez, G., and Stammes, P.: Modeling total and polarized reflectances of ice clouds: evaluation by means of POLDER and ATSR-2 measurements. Appl. Optics, 44, 4060-4073, 2005.

8. Between page 11 and 12, *"CFC overestimation of SEVIRI at high VZAs, negative values below 40° could be attributed to a similar, local-scale effect from SYNOP observations." What effect? Reason?*

Here we suggest that an effect opposite to the "cloudiness overestimation by passive satellite sensors at high VZAs", described before, can explain the opposite bias at low VZAs. According to this effect, ground-based observations tend to overestimate cloudiness, especially towards the horizon and for clouds with high vertical extent (Karlsson et al. 2003), compared to the near-nadir satellite retrievals. This statement has been rephrased to make this point clearer (page 12, lines 23-24).

# The MSG-SEVIRI based cloud property data record CLAAS-2

Nikos Benas<sup>1</sup>, Stephan Finkensieper<sup>2</sup>, Martin Stengel<sup>2</sup>, Gerd-Jan van Zadelhoff<sup>1</sup>, Timo Hanschmann<sup>2</sup>,  
Rainer Hollmann<sup>2</sup>, Jan Fokke Meirink<sup>1</sup>

<sup>1</sup>Royal Netherlands Meteorological Institute (KNMI), De Bilt, The Netherlands

5 <sup>2</sup>Deutscher Wetterdienst (DWD), Offenbach, Germany

*Correspondence to:* Nikos Benas (benas@knmi.nl)

**Abstract.** Clouds play a central role in the Earth's atmosphere, and satellite observations are crucial to monitor clouds and understand their impact on the energy budget and water cycle. Within the European Organisation for the Exploitation of Meteorological Satellites (EUMETSAT) Satellite Application Facility on Climate Monitoring (CM SAF) a new cloud  
10 property data record was derived from geostationary Meteosat Spinning Enhanced Visible and Infrared Imager (SEVIRI) measurements for the time frame 2004-2015. The resulting CLAAS-2 (CLOUD property dAtAset using SEVIRI, Edition 2) data record is publicly available via the CM SAF website (doi: 10.5676/EUM\_SAF\_CM/CLAAS/V002). In this paper we present an extensive evaluation of the CLAAS-2 cloud products, which include cloud fractional coverage, thermodynamic phase, cloud top properties, liquid/ice cloud water path and corresponding optical thickness and particle effective radius.  
15 Validation and comparisons were performed on both level 2 (native SEVIRI grid and repeat cycle) and level 3 (daily and monthly averages and histograms) data, with reference data sets derived from lidar, microwave and passive imager measurements. The evaluation results show a very good overall agreement, with matching spatial distributions and temporal variability, and small biases attributed mainly to differences in sensor characteristics, retrieval approaches, spatial/temporal samplings and viewing geometries. No major discrepancies were found. Underpinned by the good evaluation results,  
20 CLAAS-2 proves its fitness for the envisaged applications such as process studies, e.g. studies of the diurnal cycle of clouds, and the evaluation of regional climate models. The data record is planned to be extended and updated in the future.

## 1 Introduction

Clouds are of central importance for the Earth's energy budget and water cycle by modulating radiative fluxes as well as redistributing water. Consistent and stable observational data records of cloud properties are needed for climate monitoring  
25 and for evaluating the distribution of clouds in weather and climate models. This requirement is, for example, reflected in the Intergovernmental Panel on Climate Change (IPCC) statement that "clouds and aerosols continue to contribute the largest uncertainty to estimates and interpretations of the Earth's changing energy budget" (Stocker et al., 2013, Chapter 7).

Passive visible-infrared (VIS-IR) imagers provide a valuable means to observe cloud properties with high spatial resolution. The long history of such instruments has enabled the generation of several cloud data records. These include the International Satellite Cloud Climatology Project (ISCCP, Rossow and Schiffer, 1999), which is based on a combination of polar and geostationary imagers, the Pathfinder Atmospheres-Extended (PATMOS-x) data record, based on Advanced Very High Resolution Radiometer (AVHRR) measurements (Heidinger et al., 2014), data sets derived from Moderate Resolution Imaging Spectroradiometer (MODIS) measurements (Platnick et al., 2003) and the AVHRR based Cloud, albedo and radiation (CLARA) data record (Karlsson et al., 2013), created in the framework of the European Organisation for the Exploitation of Meteorological Satellites (EUMETSAT) Satellite Application Facility on Climate Monitoring (CM SAF, Schulz et al., 2009), which was recently updated (Karlsson et al., 2016).

While these datasets have global coverage, they give (apart from ISCCP) only a limited description of the temporal variability of clouds during the day. Therefore, CM SAF has been using measurements from the Spinning Enhanced Visible and Infrared Imager (SEVIRI), on board the geostationary Meteosat Second Generation (MSG) satellites, to generate the CLOUD property dAtAset using SEVIRI (CLAAS), with diurnally resolved cloud properties. The first edition of this data record (CLAAS-1) is described in Stengel et al. (2014). This data set has been used, among others, for studying the diurnal cycle of clouds (e.g. Martins et al., 2016; Pfeifroth et al., 2016) and for model evaluation (e.g. Brisson et al., 2016; Alexandri et al., 2015; ). Recently a second, reprocessed edition was released (CLAAS-2), based on updated retrieval algorithms and incorporating measurements from MSG-1, -2 and -3 satellites every 15 minutes, thus extending the time period covered (2004-2015) and increasing the temporal resolution. In particular, the 15-minute resolution now enables process studies in which individual clouds or cloud fields need to be tracked to monitor the cloud properties such as glaciation.

In this study, the CLAAS-2 cloud properties are presented and evaluated. The data record comprises cloud macro- and microphysical properties, namely cloud fractional coverage (CFC, derived from a corresponding cloud mask), cloud top location, including height (CTH), pressure (CTP) and temperature (CTT), cloud phase (CPH), which distinguishes liquid and ice clouds, and cloud water path (CWP) separately for liquid (LWP) and ice (IWP) clouds. Cloud optical thickness (COT) and particle effective radius (REF), which are used in the cloud water path computation, are also included. All these properties are available as both instantaneous data (level 2) and daily/monthly averages (level 3), along with monthly mean diurnal cycles and histograms.

The evaluation is performed by validation and intercomparison with other cloud data sets. These include (1) observations from space-based active instruments (lidar and radar), which provide the most accurate information about cloud presence in the atmosphere, (2) cloud properties derived from other passive VIS-IR satellite imagers, (3) observations of total cloud cover made at meteorological surface stations and (4) liquid water path retrieved from space borne passive microwave (MW) sensors. The evaluation is performed separately for level 2 and level 3 CLAAS-2 data, and their performance is assessed based on the different characteristics of each data set that is used as reference. Consequently, depending on the parameter being evaluated, the analysis ranges from cloud detection scores and biases to spatial distribution characteristics and time series comparisons.

This paper is organized as follows: in Sect. 2 the satellite data and algorithms used to generate the CLAAS-2 data record are described; details on the data record contents are also provided. Data sets used for the evaluation of CLAAS-2 are introduced in Sect. 3, along with the methodology used in each case. In Sect. 4 evaluation results regarding level 2 data are presented, while corresponding results for monthly aggregated (level 3) products are described in Sect. 5. Concluding remarks can be found in Sect. 6.

## 2 The CLAAS-2 data record

### 2.1 SEVIRI

SEVIRI is a 12-channel imager on the MSG geostationary satellites operated by EUMETSAT. All four planned MSG satellites, Meteosat-8, -9, -10 and -11, (also referred to as MSG-1, -2, -3 and -4, respectively), have been launched to date, with data from the first three satellites included in the CLAAS-2 data record, covering the period from January 2004 to December 2015. Apart from one high spatial resolution visible (HRV) channel, SEVIRI carries 11 channels between 0.6 and 14  $\mu\text{m}$  with a spatial sampling resolution of 3 km  $\times$  3 km at nadir and a 15-minute repeat cycle. Further information regarding the SEVIRI channels is given in Table B1 of Appendix B. The MSG satellites have been located at similar, but not exactly the same positions. Specifically, MSG-1 was positioned at 3.4° E from 2004 to 2008. Hence, even though the SEVIRI projection in level 1.5 data is aligned at 0.0° for all satellites, the positions of the individual satellites slightly change SEVIRI's viewing geometries, which has been taken into account for the generation of the CLAAS-2 data record.

In addition to the EUMETSAT nominal calibration, SEVIRI solar channels were intercalibrated with MODIS operating on board the Aqua satellite, which is considered one of the best calibrated imagers at present (Wu et al., 2013). The methodology of Meirink et al. (2013), which uses collocated, ray-matched, atmosphere-corrected, near-nadir SEVIRI and Aqua-MODIS reflectances was reapplied for our study, now using MODIS Collection 6 level 1b data as a reference and extended to cover the full CLAAS-2 time series. This included all three SEVIRI instruments that have been active, namely on MSG-1, -2 and -3. The inter-calibration with MODIS changed the reflectances by about -8% in channel 1 (0.6  $\mu\text{m}$ ), -6% (-4% for MSG-3) in channel 2 (0.8  $\mu\text{m}$ ), and +3% in channel 3 (1.6  $\mu\text{m}$ ) compared to the operational SEVIRI calibration provided by EUMETSAT. ~~The inter-calibration revealed offsets in the operational SEVIRI calibration of about -8%, -6% (-4% for MSG-3) and +3% in channels 1 (0.6  $\mu\text{m}$ ), 2 (0.8  $\mu\text{m}$ ), and 3 (1.6  $\mu\text{m}$ ), respectively.~~ Furthermore, even though the SEVIRI shortwave channels turn out to be quite stable over time, there are slight trends in the calibration coefficients. The calibration coefficients used in CLAAS-2 are reported in CM SAF (2016a). For the thermal infrared channels, the on-board calibration, as provided by EUMETSAT, was applied.

## 2.2 CLAAS-2

The CLAAS-2 dataset is the improved and extended follow-up of CLAAS-1 (Stengel et al, 2014). In the following, an overview of each CLAAS-2 retrieval algorithm is given, along with the main scientific updates applied, compared to the CLAAS-1 retrievals.

- 5 For the detection of clouds and their vertical placement, the MSGv2012 software package, developed within the framework of the Nowcasting and Very Short Range Forecasting SAF (NWC SAF), was employed. The cloud detection involves a series of spectral threshold tests, depending on, among others, the illumination (daytime, twilight, night-time, sun glint) and surface types. The algorithm classifies satellite pixels as cloud filled, cloud-free, cloud contaminated or snow/ice contaminated. Further information on the cloud detection method can be found in Derrien and Le Gléau (2005) and NWC
- 10 SAF (2013), and also in Stengel et al. (2014), regarding its implementation in CLAAS-1. Compared to the MSGv2010 algorithm version, which was applied in CLAAS-1, only minor updates were implemented. These include adaptations of detection tests that were affected by nocturnal extreme cooling conditions, which caused false cloud detections by the algorithm (NWC SAF, 2011), and corrections for coastal cloud mask artifacts, caused by high spatial standard deviation values around coastal pixels (CM SAF, 2016a). Furthermore, contrary to the default NWC SAF MSGv2012 cloud masking
- 15 algorithm, which uses  $4 \times 4$  pixels segments to reduce computational time, individual thresholds were computed for each SEVIRI pixel in CLAAS-2. The consequent increase in CLAAS-2 computation time was compensated by a higher degree of parallelization.

- Regarding the cloud vertical placement algorithm, no changes were implemented between the CLAAS-1 (MSGv2010) and CLAAS-2 (MSGv2012) versions. The algorithm, which is used for the derivation of CTH, CTP and CTT, uses input from
- 20 SEVIRI channels at 6.2, 7.3, 10.8, 12.0 and 13.4  $\mu\text{m}$ , ~~as well as the cloud type information derived from the cloud masking algorithm component~~. The spectral information is used in the simulation of corresponding radiances and brightness temperatures for overcast and clear sky conditions on a pixel basis, using the Radiative Transfer Model for TOVS (RTTOV, Saunders et al., 1999, Matricardi et al., 2004). Ancillary data of temperature and humidity profiles from ERA-Interim are also used (Dee et al., 2011). ~~Depending on the cloud type, d~~ifferent approaches are used for the derivation of CTP,
- 25 including a best fit between the simulated and the measured 10.8  $\mu\text{m}$  brightness temperatures, the H<sub>2</sub>O/IRW (Infrared Window) intercept method (Schmetz et al., 1993), and the radiance rationing method (Menzel et al., 1983). Further information on the implementation of the cloud top properties retrieval algorithm can be found in Stengel et al. (2014) and CM SAF (2016a).

- The retrieval of CPH in CLAAS-2 was based on a modified version of the Pavolonis et al. (2005) algorithm, which was
- 30 provided by the Center for Satellite Applications and Research (STAR) of the NOAA Satellite and Information Service (NESDIS). This approach constitutes a fundamental update compared to CLAAS-1, where CPH was mainly inferred from CTT and the 1.6  $\mu\text{m}$  reflectance. According to the new retrieval scheme, a number of spectral tests are performed in a specific order, involving measurements from SEVIRI channels at 6.2, 8.7, 10.8, 12.0 and 13.4  $\mu\text{m}$ , as well as clear and

cloudy sky IR radiances and brightness temperatures, calculated using RTTOV. The algorithm initially yields one of the following cloud types: liquid, supercooled, opaque ice, cirrus, overlap, and overshooting, which are then further condensed to liquid (former two) and ice (latter four) phase. Details on the algorithm can be found in CM SAF (2016b).

The retrieval of cloud optical and microphysical properties was based on the Cloud Physical Properties (CPP) algorithm (Roebeling et al., 2006; CM SAF 2016b). The algorithm uses SEVIRI's visible (0.6  $\mu\text{m}$ ) and near-infrared (1.6  $\mu\text{m}$ ) measurements to retrieve COT and REF by applying the classical Nakajima and King (1990) approach. CPP is based on look-up tables (LUTs) of top-of-atmosphere (TOA) reflectances simulated by the Doubling Adding KNMI (DAK) radiative transfer model (Stammes, 2001), which has been frequently used in the past for numerous cloud and aerosol radiative transfer applications (e.g., de Graaf et al., 2012; Tilstra et al., 2012). The setup of these LUTs is provided in Table 1, which also contains information on the underlying single scattering calculations for liquid and ice cloud particles, as well as information on the assumed shape and properties of ice particles. Absorption by atmospheric trace gases is taken into account based on Moderate Resolution Atmospheric Transmission code (MODTRAN4 Version 2; Anderson et al., 2001) simulations. LWP and IWP are calculated following Stephens (1978):

$$LWP = \frac{2}{3} \rho_l r_e \tau; \quad IWP = \frac{2}{3} \rho_i r_e \tau \quad (1)$$

where  $\rho_l$  and  $\rho_i$  are the densities of water and ice, respectively,  $r_e$  is REF and  $\tau$  is COT. No retrievals are performed for solar zenith angles (SZAs) or viewing zenith angles (VZAs) larger than  $84^\circ$ , due to high uncertainties in the retrieved properties at these angles. The main updates of CPP, compared to CLAAS-1, include the generation of new LUTs, with an extension in the range of SZAs and VZAs, and the number and range of REF, as well as the inclusion of observational sea-ice (OSI SAF, 2016) and ERA-Interim snow cover data to better characterize the surface albedo, which is for all other surface types taken from MODIS (Moody et al., 2005).

CLAAS-2 level 2 data contain 15-minute SEVIRI pixel-based retrievals from 2004 to 2015. Level 3 data contain daily and monthly aggregated products. For the cloud parameters considered here, the daily aggregation was done by linear averaging of all valid retrievals (available on the native SEVIRI projection), into  $0.05^\circ \times 0.05^\circ$  grid boxes. Daily means were then further averaged to monthly means, whereby at least 20 daily mean values were required for the estimation of monthly average CFCs. It should be noted, however, that this threshold was only applied as a fail-safe mechanism; in practice, apart from the first month of the CLAAS-2 time series (January 2004), no gaps are present in the monthly mean data. CFC was calculated from the cloud mask by counting cloud-free pixels as 0, and both cloud-contaminated and cloud-filled pixels as 1. In addition to the 'day-and-night' CFC, separate averages for daytime and nighttime were computed. Level 3 products of cloud LWP and IWP (including COT and REF) are available during daytime only, both as cloudy-sky means and all-sky means. Apart from the regular monthly aggregated products, monthly mean diurnal cycles have been calculated by averaging all daily mean diurnal cycles in a month. In order to retain a sufficient number of observations in each grid box, these monthly mean diurnal cycles have been prepared on a coarser spatial grid of  $0.25^\circ \times 0.25^\circ$ . In addition to the mean monthly properties, monthly histograms are composed, collecting the number of occurrences of cloud properties. Collected are CWP,

CTP, CTT, COT and REF in one-dimensional, cloud-phase-separated, spatially-resolved histograms of  $0.05^\circ \times 0.05^\circ$  spatial resolution, and combinations of CTP and COT in two-dimensional, cloud-phase-separated, spatially-resolved histograms of  $0.25^\circ \times 0.25^\circ$  spatial resolution. The binning of the histograms is as given in Table 3 of Stengel et al. (2014). The REF histograms, which were not included in CLAAS-1, have bin borders of: 3, 6, 9, 12, 15, 20, 25, 30, 40, 60, 80  $\mu\text{m}$ .

5 The CLAAS-2 data record is (as all CM SAF climate data records) freely available online via [http://dx.doi.org/10.5676/EUM\\_SAF\\_CM/CLAAS/V002](http://dx.doi.org/10.5676/EUM_SAF_CM/CLAAS/V002), including comprehensive documentation and auxiliary data facilitating work with the data record. CM SAF's ([www.cmsaf.eu](http://www.cmsaf.eu)) main task is to generate and provide in a sustained effort Climate Data Records (CDRs) derived from operational meteorological satellites. In particular CDRs for components of the global energy budget and water cycle are the main focus. During the full generation and delivery process CM SAF adheres  
10 to the international Global Climate Observing System (GCOS) guidelines. Thus, CM SAF is applying the highest standards to make the resulting data records suitable for the analysis of climate variability and the detection of climate trends.

### 3 Data sets and methodology used for evaluation

In this section, the data sets used as references for the evaluation of CLAAS-2 are described, along with the methodology used in each case. Reference data sets comprise measurements from lidar, radar, microwave and passive space borne sensors,  
15 as well as surface observations.

#### 3.1 CALIOP

The Cloud-Aerosol Lidar with Orthogonal Polarization (CALIOP) is a lidar instrument on board the CALIPSO (Cloud-Aerosol Lidar and Infrared Pathfinder Satellite Observation) satellite, providing cloud and aerosol profile information since August 2006 (Winker et al. 2009). CALIOP products are retrieved based on backscattered signal at 1064 nm and 532 nm,  
20 available at horizontal and vertical resolutions of 333 m and 30-60 m respectively. They include cloud phase and type for up to 10 cloud layers per column, as well as CTP, CTH and CTT at each layer top.

The CALIOP level 2 layered cloud products (CAL\_LID\_L2\_05kmCLay-Prov) in 5 km resolution (data set versions 3-01, 3-02 and 3-30) were used here. Among five different ~~options~~ CALIOP along-track resolutions available, namely 333 m, 1 km, 5 km, 20 km and 80 km, the 5 km resolution was selected as the closest to the CLAAS-2 level 2 resolution, while it also  
25 offers higher confidence in cloud detection and identification, compared to the original footprint resolution, by horizontally averaging up to 80 km of measurements (Winker et al., 2009). For the CLAAS-2 level 2 validation, a data set of collocated CALIOP and CLAAS-2 measurements was created, comprising 100 million matchups between 2006 and 2015. Spatial collocation was performed using a nearest neighbour approach while temporal collocation was achieved by matching each CALIOP measurement time with the acquisition time of the closest SEVIRI scanline. This approach allows for maximum  
30 time and space differences of 7.5 minutes and 5 km, respectively.



CLAAS-2 level 2 products were validated against corresponding CALIOP products (Sect. 4.1); for discrete variables, namely cloud mask (cloudy/clear) and CPH (water/ice), validation was based on statistical scores, including Probability of Detection (POD), False Alarm Ratio (FAR), hitrate and the Hanssen-Kuiper skill score (KSS), while downscaled spatial distributions were also compared. The formulas used for the computation of these scores are the following:

$$5 \quad \text{POD for event 1, 2: } \frac{n_{11}}{n_{11} + n_{21}}, \frac{n_{22}}{n_{22} + n_{12}} \quad (2)$$

$$\text{FAR for event 1, 2: } \frac{n_{12}}{n_{11} + n_{12}}, \frac{n_{21}}{n_{22} + n_{21}} \quad (3)$$

$$\text{Hitrate: } \frac{n_{11} + n_{22}}{n_{11} + n_{12} + n_{21} + n_{22}} \quad (4)$$

$$\text{KSS: } \frac{n_{11}n_{22} - n_{21}n_{12}}{(n_{11} + n_{21})(n_{12} + n_{22})} \quad (5)$$

In the above formulas,  $n_{ij}$  is the number of cases where CLAAS-2 reports event  $i$  and CALIOP reports event  $j$  (Table 2).

10 Events correspond to cloudy and clear cases for cloud mask and water or ice clouds for CPH.

It should finally be noted that CALIOP's higher sensitivity to high and optically thin clouds, compared to SEVIRI, is an important factor affecting the validation results. In order to address this sensitivity difference and investigate the accuracy of CLAAS-2 products, comparisons were repeated by sampling the CALIOP profiles at successive layers below the cloud top, using different thresholds for the integrated COT of these layers.

## 15 **3.2 DARDAR**

The DARDAR (lidar/radar) data set was created using a synergistic approach which combines data of Cloudsat Cloud Profiling Radar (CPR) reflectivity, CALIOP lidar attenuated backscatter and MODIS infrared radiance measurements, to retrieve ice cloud properties, including COT, REF and IWP. The retrieval is based on an optimal estimation approach, which ensures a smooth transition between regimes where different instruments are sensitive (Delanoë and Hogan, 2008, 2010).

20 The products have the same vertical resolution as CALIOP (30-60 m) and the horizontal resolution of CPR (700 m × 700 m). DARDAR data of ice COT and IWP were used for the validation of corresponding CLAAS-2 level 2 products. The DARDAR data used here comprises overpasses from the SEVIRI disk during January and July 2008. Extreme illumination geometries were excluded by selecting only retrievals at SZAs below 75°. Furthermore, DARDAR profiles which consist of ice CPH only were considered, and in each SEVIRI pixel a single profile was included only when all profiles in this pixel  
25 had the same CPH.

## **3.3 MODIS**

MODIS is an advanced imaging spectroradiometer operating on board NASA's Terra and Aqua satellites since February 2000 and July 2002, respectively (Salomonson et al., 1989). Both Terra and Aqua orbits are sun synchronous and timed so that they cross the equator at 10:30 and 13:30 local solar times, in a descending and ascending node, respectively. With a

viewing swath width of 2330 km, MODIS covers every point on the Earth's surface in 1 to 2 days, acquiring data in 36 spectral bands.

Since MODIS is among the most advanced passive imagers in space, and has been operating during the entire CLAAS-2 time range, cloud products from the latest MODIS Collection (C006, Platnick et al., 2015) were used here as a reference. For level 2 intercomparisons (Sect. 4.3), a specific MODIS granule was selected as case study, and the MODIS and SEVIRI grids were sampled to a common regular latitude-longitude grid. For level 3 evaluation (Sect. 5.3), the CLAAS-2 monthly products were downsampled from their  $0.05^\circ \times 0.05^\circ$  resolution to the MODIS  $1^\circ \times 1^\circ$  grid by spatial averaging. Since both level 2 and 3 MODIS data products are available separately from Terra and Aqua satellites, and CLAAS-2 level 3 monthly mean products are computed by averaging all SEVIRI time slots (daytime-only slots for optical properties), Terra and Aqua MODIS monthly products were also averaged, to best mimic this CLAAS-2 diurnal averaging. In the CFC and CPH cases, however, only Aqua MODIS data were used, due to a Terra MODIS band 29 ( $8.6 \mu\text{m}$ ) radiometric calibration drift issue, which has affected Collection 6. This band is used in the CFC and CPH retrieval algorithms (Baum et al. 2012), where significant biases were found in the monthly time series, extending back to earlier than 2010. Furthermore, as in the optical properties case, only daytime CFC and CPH data were compared against MODIS. It should also be noted that, for consistency purposes, cloud optical properties retrievals based on MODIS band 6 ( $1.6 \mu\text{m}$ ) were used in these intercomparisons.

### 3.4 SYNOP

Total cloud cover data from surface synoptic observations (SYNOP) were used for the evaluation of CLAAS-2 level 3 monthly CFC. SYNOP data span the entire CLAAS-2 period (2004-2015) and originate from all land areas of the SEVIRI disk, with higher density of stations in European countries. The SYNOP data used for the validation have been taken from the local DWD archive of collected global SYNOP reports following the guidance of the Guide to Meteorological Instruments and Methods of Observations (Jarraud, 2008). In order to ensure data quality and consistency, only SYNOP reports provided by manned airport stations were taken into account.

Monthly averaged CFC values from SYNOP stations were estimated based on corresponding daily averages. The latter were calculated when at least 6 instantaneous measurements were available. Additionally, as in the CLAAS-2 level 3 case, at least 20 daily mean CFC values were required for the estimation of monthly averages. Except for the level of agreement between the SYNOP and collocated CLAAS-2 level 3 CFC products, the dependency of this agreement on the SEVIRI VZA was also examined (Sect. 5.1).

### 3.5 Microwave imagers

MW-based retrievals from the University of Wisconsin (UWisc) LWP climatology were used for the validation of CLAAS-2 level 3 LWP. This dataset, described in detail in O'Dell et al. (2008), was created based on retrievals from various MW sensors, including the Special Sensor Microwave Imager (SSM/I), the Tropical Rainfall Measuring Mission (TRMM) and

the Advanced Microwave Scanning Radiometer for Earth Observing System (AMSR-E). The UWisc data set provides monthly mean diurnal cycles over global oceans at  $1^\circ \times 1^\circ$  spatial resolution, during the period 1988-2008. LWP estimates are reported to have an accuracy of 15% to 30% (O'Dell et al., 2008).

It should be noted that, since MW measurements are not sensitive to the presence of ice clouds, the validation was limited to areas with sufficiently low ice cloud fraction. In the SEVIRI disk this requirement is fulfilled over the marine stratocumulus (Sc) area of South Atlantic, off the Namibian coast. Specifically, the region defined by the  $20^\circ$ - $10^\circ$ S and  $0^\circ$ - $10^\circ$ E latitude-longitude boundaries was selected for this purpose. Validation includes both monthly mean time series and average diurnal cycle intercomparisons of all-sky LWP, computed by averaging pixel values from the Sc study region (Sect. 5.2).

## 4 Level 2 evaluation

In this section, validation results of CLAAS-2 level 2 products against CALIOP and DARDAR are described. Furthermore we discuss comparisons of CLAAS-2 level 2 products with MODIS data.

### 4.1 Validation with CALIOP

Based on all collected CLAAS-2 level 2 and CALIOP collocations, an overall cloud POD of 87.5% was found, while the corresponding FAR was 16.9% and the hitrate reached 80.9%. Differences between day and night collocations were minor, while the cloud POD was significantly higher over sea compared to land, at the cost of an also much higher FAR.

Corresponding scores for CPH were 91.6% and 74.9% (liquid and ice POD), and 29.8% and 6.7% (liquid and ice FAR), with an overall CPH hitrate of 81.4%. Both low values of ice cloud POD and high values of liquid cloud FAR should be attributed to CALIOP's higher sensitivity to high and optically thin clouds. In fact, when these clouds are excluded from the analysis, ice cloud scores acquire higher values, with ice POD becoming similar to the liquid POD, while liquid cloud FAR is reduced to 10.0% when the CALIOP phase was sampled at a COT of 0.2 below the cloud top. These results are summarized in Table 3.

This ~~difference in~~ sensitivity ~~mismatch between CLAAS-2 and CALIOP~~ was further analysed by using a varying CALIOP total column COT as a threshold for distinguishing cloud free from cloudy scenes. Hence, all CALIOP scenes with COT less than this threshold were set as cloud free. setting as cloud free, scenes with CALIOP total column COT measurements smaller than a certain threshold. Results are shown in Fig. 1a, with the COT threshold in the x-axis. It is obvious that as the COT threshold used to distinguish clear and cloudy CALIOP measurements increases, both POD and FAR increase. The POD increases because optically thin clouds, which are likely not to be detected by SEVIRI, are also excluded from CALIOP and the number of scenes where both CALIOP and CLAAS-2 detect clouds increases. However, as the COT threshold increases, also some clouds that are detected by SEVIRI are excluded from CALIOP; such cases cause an increase in FAR. This is the result of two simultaneous effects, whereby optically thin CALIOP clouds not detected by SEVIRI are

~~reset to cloud free scenes, thus increasing the cloud POD, and optically thin CALIOP clouds detected by SEVIRI are also reset to cloud free, leading to an increased FAR.~~ These effects combined cause the hitrate and KSS to peak at  $COT \approx 0.05$ .

The effect of using as reference the CPH at the layer where the integrated COT (ICOT) exceeds a certain threshold, instead of the uppermost layer, is shown in Fig. 1b. Applying this ICOT threshold leads to an increase in ice cloud POD, since thin ice clouds detected by CALIOP but not by SEVIRI are excluded. There are two ways how the liquid POD can be influenced when excluding a thin CALIOP ice cloud and instead comparing against a liquid CALIOP cloud located below: If the thin ice cloud was incorrectly reported as liquid by CLAAS-2, the liquid POD would increase whereas it would decrease if the cloud was correctly reported as ice by CLAAS-2. It was found that the second case occurrences increased with ICOT three times stronger than the first, leading to the decrease in liquid cloud POD shown in Fig. 1b.

Figure 2 shows the spatial distributions of cloud fraction and ice cloud fraction, estimated from all collocated CLAAS-2 level 2 and CALIOP measurements. The maps were created by remapping matchups to a regular  $1.5^\circ \times 1.5^\circ$  grid and averaging within each grid box. Large scale patterns between the two data sets are similar for both cloud fraction and phase. There is a tendency for CLAAS-2 to overestimate cloud fraction over the northern and southern Atlantic, as well as the Indian Ocean, which may be related to the high VZAs over these areas (cf. Reuter et al. 2009). On the other hand, cloud fraction in the tropics is underestimated by CLAAS-2, probably due to the frequent presence of cirrus clouds in this area, which are more likely to be detected by CALIOP (Sun et al. 2011). The phase agreement is overall very good, with slightly less ice clouds being reported by CLAAS-2 over Africa and the central Atlantic, which is consistent with the difference in cloud fraction over the same areas.

Taking the CALIOP CTT as reference, the relation of CTT and CPH was also examined (Fig. 3). The agreement is excellent in both liquid and ice cloud histograms, when using  $ICOT=0.2$  as a threshold layer for CALIOP CTT and CPH selection. It should be noted that the CLAAS-2 histogram extensions above  $0^\circ\text{C}$  for ice clouds (red dashed line in Fig. 3) and below  $-42^\circ\text{C}$  for liquid clouds (red solid line in Fig. 3) should be attributed to the fact that the x-axis CTT binning in this figure comes from CALIOP. The CLAAS-2 CTT is always below  $0^\circ\text{C}$  for ice clouds and above  $-42^\circ\text{C}$  for liquid clouds. Hence, these histogram extensions are related to CALIOP retrieving higher CTT (former case) or lower CTT (latter case) than CLAAS-2.

If CLAAS-2 CTT was used instead, such cases would not be allowed by the retrieval algorithm.

The CLAAS-2 cloud top properties, namely CTH, CTP and CTT, were directly compared to corresponding CALIOP data of the uppermost cloud layer detected. These comparisons revealed an underestimation of CTH by CLAAS-2, and consequent overestimations of CTP and CTT. These results should also be attributed to the discrepancies in high optically thin cloud detection between the two data sets. In fact, when examining these biases using varying CALIOP cloud top layers, based on different ICOT threshold values, a strong influence was found (Fig. 4). All biases acquire their minimum absolute values at an ICOT threshold of about 0.3-0.5 and their signs are reversed as the ICOT of CALIOP cloud top layers excluded is increased towards 2.0. The spread of CLAAS-2 compared to CALIOP data is also reduced, as can be seen from the bias-corrected Root Mean Square Error (bc-RMSE), represented as error bars in Fig. 4.

In contrast to ~~binary-level 2 variables like~~ cloud mask and cloud phase variables, which acquire values of only 0 or 1, cloud top variables are continuous so that a correlation analysis can be performed. The results are shown as scatter plots in Fig. 5. The overall correlation is strong in all cloud top products, with Pearson correlation coefficients ranging between 0.84 and 0.88. The least squares fit slopes are below 1, which also reflects the underestimation in CTH and overestimation in CTP and CTT of high clouds by CLAAS-2.

## 4.2 Validation with DARDAR

Figure 6a shows the CLAAS-2 vs. DARDAR ~~single-layer~~ ice COT comparison. The distribution contours show the number of points enclosed, e.g., the black area (central contour) encloses the 20% of bins with the largest density containing the largest density or 20% largest density of observations. The distribution is clearly correlated and lies along the 1:1 line. However, the remaining 25% of the observations outside of the density contours (not shown in the figure) are so much scattered ~~in parameter space~~ that the total correlation remains weak (0.33).

The IWP (Fig. 6b) is proportional to the product of ice COT and REF, as expressed in Eq. (1). Hence, the transition of the ice COT correspondence along the 1:1 line (Fig. 6a) into the curved ~~IWP 2-D occurrence~~ distribution of Fig. 6b should be attributed to differences in ice REF. This curved distribution for low IWP values also appears in results from Eliasson et al. (2013), where IWP from MODIS and PATMOS-x is compared with DARDAR. Figure 6c shows that the range of IWP values and the~~The occurrence~~ distribution of occurrences and dynamic in this range for each of the individual data sets, however, are similar (Fig. 6c) between DARDAR and CLAAS-2.

~~The distributions look similar to the ones presented in Eliasson et al. (2013), with the curve for low IWP values as seen in their Figure 6 for MODIS and PATMOS-x. These results show highlight the difficulty in interpreting that~~ an evaluation of passive versus active instruments ~~is difficult to interpret due to~~. The main reasons for this difficulty include the different microphysical assumptions applied in the retrievals, as well as the difference between column-averaged ~~measurements~~ (but weighted to the top of the cloud) retrievals from variable viewing geometries for the passive instrument versus profile information ~~and variable viewing geometries vs. the from~~ near nadir view ~~for~~ the active instruments.

## 4.3 Comparison with MODIS

For the level 2 CLAAS-2 comparison with MODIS Collection 6, one Terra MODIS granule is shown as a case study. The granule on 20 June 2008, from 10:50 to 10:55 UTC was selected, covering the largest part of Europe, since it fulfilled a number of criteria, including a balanced presence between low and high, liquid and ice, and thin and thick clouds, as well as relatively low SZAs. The time difference between the two data sets was also minimized, by selecting the 10:45 UTC SEVIRI time slot, which covered Europe at around 10:56 UTC.

Figure 7 shows histograms of CLAAS-2 and MODIS COT, REF and CWP from this granule, separately for liquid and ice clouds, created using only collocations where CPH was the same in both data sets. The liquid COT histograms reveal a good agreement, while ice COT is slightly larger in CLAAS-2 than in MODIS. Relative peaks at COT=100 should be attributed to

the fact that COT retrievals greater than 100 are set equal to 100, causing the relatively higher number of pixels found with this value. The MODIS 1.6  $\mu\text{m}$  and 2.1  $\mu\text{m}$  REF retrievals yield slightly different histograms. Considering that the CLAAS-2 products are based on 1.6  $\mu\text{m}$  measurements, it is somewhat surprising that the CLAAS-2 REF agrees better with the MODIS 2.1  $\mu\text{m}$  product than the 1.6  $\mu\text{m}$  especially in the liquid clouds case. For ice clouds, CLAAS-2 acquires overall lower REF, which is most probably related to the choice of ice particle habits: i.e. severely roughened monodisperse hexagonal columns for CLAAS-2 versus severely roughened aggregated columns with a gamma size distribution (Yang et al., 2013) for MODIS C6. Consistent with the results of the REF intercomparison, the agreement for LWP is better than for IWP.

## 5 Level 3 evaluation

10 This section covers the evaluation of CLAAS-2 level-3 products, namely daily and monthly aggregations as well as monthly mean diurnal cycles.

### 5.1 Validation with SYNOP

The comparison of CLAAS-2 monthly mean CFC data with corresponding SYNOP observations showed an overall good agreement, with an average (over all SYNOP stations) CLAAS-2 – SYNOP bias of 3.7%, never exceeding 7.5%. This bias, however, is positive for the entire time series, as a consequence of the well-known effect of cloudiness overestimation by passive satellite sensors at high VZAs (e.g., Maddux et al., 2010) in combination with most SYNOP stations being located in Central Europe, away from the SEVIRI nadir view point.

This effect was verified by a more detailed analysis on the dependency of CFC bias on VZA. The results of this analysis are shown in Fig. 8, where CFC bias values have been averaged in 10° VZA bins, along with values of the bc-RMSE, which gives a measure of the precision of CLAAS-2 observations, and the number of observations available from SYNOP. The bias is negative for VZAs below 40°, becoming positive for larger angles. While positive bias values are explained by the CFC overestimation of SEVIRI at high VZAs, negative values below 40° could be attributed to a similar, local-scale effect from SYNOP-observations, whereby ground-based observations tend to overestimate cloudiness (especially towards the horizon), compared to the low VZA retrievals from SEVIRI. This scenery effect leads to an overestimation of CFC by SYNOP due to the obscuring of cloud-free spaces by convective clouds with high vertical extent (Karlsson, 2003). However, the small number of observations in this VZA range is prohibitive for drawing any further conclusions. In the 30°-60° VZA range, on the other hand, the best accuracy and precision of CLAAS-2 CFC are achieved. Northern mid-latitudes (i.e. Europe) dominate this VZA range, where the greatest number of observations can also be found, thus enhancing the robustness of the results.

## 5.2 Validation with UWisc

Figure 9a shows the time series plot of the monthly all-sky LWP at 12:00 UTC from CLAAS-2 and UWisc, calculated over the marine Sc region west of Namibia (0-10° E, 10-20° S). The two data records exhibit similar seasonal characteristics, with the largest differences appearing almost every year in August and September, when CLAAS-2 acquires lower values compared to the UWisc all-sky LWP. This characteristic should be attributed to the presence of absorbing aerosols over the clouds, originating from biomass burning activities during this season; these overlying aerosols cause a negative bias in the LWP retrieval (Haywood et al. 2004).

The average diurnal cycle of all-sky LWP over the marine Sc region from CLAAS-2 and UWisc is shown in Fig. 9b. In order to ensure the equivalence of results, all spatial averages computed from cases with more than 50% missing values were excluded from the analysis, leading to the absence of night time and twilight hours from the plot. Both CLAAS-2 and UWisc show the reduction in all-sky LWP throughout the day, in the 10-hour part of the diurnal cycle depicted in Fig. 9b. The smoothness of the UWisc curve should be attributed to its derivation as a fit to satellite data from various overpass times (O'Dell et al. 2008). Compared to UWisc, CLAAS-2 exhibits overall similar values, except before sunset, with an increase that may be a retrieval artifact related to illumination geometry (high SZAs).

## 5.3 Comparison with MODIS

Figure 10 shows the intercomparison of CLAAS-2 and MODIS level 3 spatial distributions, computed by averaging monthly data from the entire CLAAS-2 period, along with their differences. In the CFC and CPH cases (Fig. 10a and c), MODIS data are based on the cloud mask product, which is affected by the Terra calibration drift issue. Hence, an intercomparison only with Aqua MODIS data was performed in these two cases, as described in Sect. 3.3.

The two data sets have similar CFC spatial patterns (Fig. 10a), with lower values from CLAAS-2 appearing over central and western Africa and higher towards the edge of the disk. This pattern of differences should probably be attributed to the viewing geometry of SEVIRI, with increasing viewing angles from the nadir of Meteosat to the edges of the SEVIRI disk, which would also lead to increased cloud cover retrieval, compared to the MODIS typical range of viewing angles (cf. Figure 2). In addition, the difference tends to have an opposite sign over land and ocean, most pronounced e.g. over South America, Europe and the Red Sea. Figure 10b shows the CTH distributions and differences. Overall, CLAAS-2 tends to estimate higher cloud top heights, with the exceptions of central Africa and the Sahara desert, where for the latter region CFC is minimal. The southern Atlantic marine Sc clouds are also placed slightly lower in CLAAS-2. The fraction of liquid clouds, expressed in CPH, is shown in Fig. 10c. As expected, patterns are similar to the CTH case, with liquid clouds obviously prevailing at lower CTHs. Compared to MODIS, CLAAS-2 retrieves more ice clouds at the eastern and western edges of the disk, and more liquid clouds around the 60° S zone. Figure 10d shows the spatial distribution of the all-sky LWP from CLAAS-2, MODIS and their difference. In both data sets, high all-sky LWP values appear mainly over the South and North Atlantic and Europe, while the Sc region west of South Africa is also highlighted. In terms of differences, there is

an overall tendency for opposite signs over land and ocean, as in the CFC case. The all-sky IWP spatial distribution, depicted in Fig. 10e, reveals good agreement in terms of spatial features between CLAAS-2 and MODIS, with high values over Central Africa, the Inter-Tropical Convergence Zone (ITCZ) and South America. Similar patterns appear in the differences map, suggesting a proportionality to the absolute all-sky IWP values. CLAAS-2 generally acquires lower values than MODIS, with few exceptions including the area near Antarctica, where sea ice might be causing artifacts in the CLAAS-2 retrieval. The lower CLAAS-2 IWP is consistent with the level-2 comparisons in Fig. 7, demonstrating that it is mainly explained by differences in the effective radius retrievals.

Overall, the intercomparison of temporally averaged distributions shows that CLAAS-2 and MODIS are in good agreement. In all the variables shown in Fig. 10, additional possible reasons causing differences between the data sets include the diurnal variability of clouds, which is not fully captured by MODIS, as well as differences in cloud masking algorithms and the spatial averaging processes being used for the production of level 3 data.

Figure 11 shows the time series of the area-weighted averages of CLAAS-2 and MODIS level 3 cloud products over the 45° W-E and S-N region. This area was selected instead of the entire SEVIRI disk to ensure consistency of the time series of the daytime products in all seasons.

The daytime CFC time series (Fig. 11a) shows that CLAAS-2 and MODIS are in good agreement regarding both seasonal cycle and absolute values, also considering their differences in temporal sampling (averaging of daytime vs. once-per-day retrievals). Both time series also appear stable throughout the 12-year period examined, with no significant trend. The tendency of CLAAS-2 to acquire higher CTH values compared to MODIS, presented in Fig. 10b, is verified by the corresponding time series (Fig. 11b); while the seasonality of CTH is similar in both data records, the mean CTH difference between them is ~300 m. It is worth noting, however, that this difference decreases after 2013, due to a slight decrease in CLAAS-2 CTH. This change, not appearing in MODIS data, should probably be attributed to the transition from MSG-2 to MSG-3, which occurred in January 2013, but further investigation is required to confirm this. A similar feature appears in the CPH time series (Fig. 11c), with very good agreement in terms of seasonal variation and absolute values, and a transition of CLAAS-2 from slightly lower to slightly higher values, compared to MODIS, in 2013. The CLAAS-2 monthly all-sky LWP is systematically higher than MODIS by  $0.002 \text{ kg m}^{-2}$  on average (Fig. 11d). This should be attributed to the positive differences over the Atlantic ocean, which covers a large part of the 45° W-E and S-N region. Furthermore, no significant change or trend appears in either data set. This is not the case, however, in the all-sky IWP, where in both CLAAS-2 and MODIS a decreasing trend appears during the second half of the time series (Fig. 11e). While further investigation of this feature is beyond the scope of this study, its presence and consistency in both data records suggests an origin beyond sensor or calibration issues. The mean difference between the two data sets is around  $-0.005 \text{ kg m}^{-2}$  throughout the time series.



6 Summary

This study focused on the validation and intercomparison of the recently released cloud property data record CLAAS-2 by CM SAF, based on measurements from the SEVIRI sensor on board geostationary satellites MSG-1, 2 and 3. The main characteristics of the retrieval algorithms used for the creation of CLAAS-2 were described, along with their updates compared to the first CLAAS edition.

A variety of reference datasets from different sensors and based on different retrieval approaches were used to evaluate and intercompare the CLAAS-2 retrievals at all possible processing levels. Validation was based on active sensors, which are considered the most accurate measurements of cloud properties in the atmosphere, as well as on ground based observations. Intercomparisons were made with MODIS, which is one of the most advanced passive sensors whose retrievals are similar to those used in CLAAS-2.

The results revealed overall good agreement between CLAAS-2 and the reference data sets. While no major discrepancies were found, the differences reported can be attributed to various factors, ranging from different retrieval approaches (e.g. profile retrievals from active sensors vs. column integrated retrievals from passive sensors), different microphysical assumptions in otherwise similar methodologies (e.g. between CLAAS-2 and MODIS), and differences in spatial and temporal samplings, as well as viewing geometries. Considering all these factors, the results presented here confirm the reliability and stability of CLAAS-2 data.

In view of the present findings, CLAAS-2 can be considered as a valuable source of data for studies on clouds and their role in the (regional) climate system. Making use of the advantages of a geostationary imager, it combines high spatial and temporal resolutions, rendering the data products suitable for both local and continental scale studies, at time frames ranging from sub-hourly processes to interannual variability.

Recently, EUMETSAT and the co-funding national meteorological services secured continuation of this work, and a third edition of CLAAS is planned for release around 2021, benefiting from potentially improved calibration, further enhanced retrievals schemes, and a prolonged time coverage.

## Appendix A: List of abbreviations

	AMSR-E	Advanced Microwave Scanning Radiometer for Earth Observing System
	AVHRR	Advanced Very High Resolution Radiometer
	bc-RMSE	bias corrected Root Mean Square Error
5	CALIOP	Cloud-Aerosol Lidar with Orthogonal Polarization
	CALIPSO	Cloud-Aerosol Lidar and Infrared Pathfinder Satellite Observation
	CDR	Climate Data Record
	CFC	Cloud Fractional Coverage
	CLAAS	Cloud property dAtAset using SEVIRI
10	CLARA	CM SAF cLoud, Albedo and surface RAdiation dataset
	CM SAF	Satellite Application Facility on Climate Monitoring
	COT	Cloud Optical Thickness
	CPH	Cloud Phase
	CPP	Cloud Physical Properties
15	CPR	Cloud Profiling Radar
	CTH	Cloud Top Height
	CTP	Cloud Top Pressure
	CTT	Cloud Top Temperature
	CWP	Cloud Water Path
20	DAK	Doubling Adding KNMI
	DARDAR	raDAR/liDAR
	ERA-Interim	ECMWF Reanalysis Interim Dataset
	ECMWF	European Centre for Medium-Range Weather Forecasts
	EUMETSAT	European Organisation for the Exploitation of Meteorological Satellites
25	FAR	False Alarm Ratio
	GCOS	Global Climate Observing System
	HRV	High Spatial Resolution Visible Channel
	ICOT	Integrated COT
	IPCC	Intergovernmental Panel on Climate Change
30	IR	Infrared
	ISCCP	International Satellite Cloud Climatology Project
	ITCZ	Inter-Tropical Convergence Zone
	IWP	Ice Water Path

	KSS	Hanssen-Kuiper skill score
	LUT	look-up table
	LWP	Liquid Water Path
	MODIS	Moderate Resolution Imaging Spectroradiometer
5	MODTRAN	Moderate Resolution Atmospheric Transmission
	MSG	Meteosat Second Generation
	MW	Microwave
	NASA	National Aeronautics and Space Administration
	NESDIS	NOAA Satellite and Information Service
10	NOAA	National Oceanic and Atmospheric Administration
	NWC SAF	Nowcasting and Very Short Range Forecasting Satellite Application Facility
	OSI SAF	Ocean and Sea Ice Satellite Application Facility
	PATMOS-x	Pathfinder Atmospheres-Extended
	POD	Probability of Detection
15	REF	Effective Radius
	RTTOV	Radiative Transfer Model for TOVS
	SEVIRI	Spinning Enhanced Visible and Infrared Imager
	SSM/I	Special Sensor Microwave Imager
	STAR	Center for Satellite Applications and Research
20	SYNOP	Surface Synoptic Observations
	SZA	Solar Zenith Angle
	TOA	Top-of-Atmosphere
	TOVS	TIROS Operational Vertical Sounder
	TRMM	Tropical Rainfall Measuring Mission
25	UWisc	University of Wisconsin
	VIS	Visible
	VZA	Viewing Zenith Angle

**Appendix B: Spectral characteristics of SEVIRI channels**

**Table B1: MSG SEVIRI channels. Specifications include channel number, central wavelength (μm) and nominal spectral band width (μm).**

Channel	Central wavelength	Spectral band width
HRV	N/A	about 0.4-1.1
1	0.635	0.56-0.71
2	0.81	0.74-0.88
3	1.64	1.50-1.78
4	3.92	3.48-4.36
5	6.25	5.35-7.15
6	7.35	6.85-7.85
7	8.70	8.30-9.10
8	9.66	9.38-9.94
9	10.80	9.80-11.80
10	12.00	11.00-13.00
11	13.40	12.40-14.40

5

**Acknowledgements**

The authors thank Dr. Andrew Heidinger (NOAA) for the provision of the modified version of the Pavolonis et al. (2005) cloud phase algorithm.

10 This work was performed within CM SAF funded by EUMETSAT in cooperation with the national meteorological services of Germany, Sweden, Finland, The Netherlands, Belgium, Switzerland and United Kingdom.

**References**

Alexandri, G., Georgoulas, A. K., Zanis, P., Katragkou, E., Tsikerdekis, A., Kourtidis, K., and Meleti, C.: On the ability of  
15 RegCM4 regional climate model to simulate surface solar radiation patterns over Europe: an assessment using satellite-based observations, Atmos. Chem. Phys., 15, 13195-13216, doi:10.5194/acp-15-13195-2015, 2015.

- Anderson, G. P., Berk, A., Acharya, P. K., Matthew, M.W., Bernstein, L. S., Chetwynd, J. H., Dothe, H., Adler-Golder, S. M., Ratkowski, A. J., Felde, G. W., Gardner, J. A., Hoke, M. L., Richtsmeier, S. C., and Jeong, L. S.: MODTRAN4 version 2: radiative transfer modeling, *Proceedings of SPIE*, 4381, 455–459, 2001.
- Baum, B. A., Menzel, W. P., Frey, R. A., Tobin, D. C., Holz, R. E., Ackerman, S. A., Heidinger, A. K., and Yang, P.: MODIS Cloud-Top Property Refinements for Collection 6, *J. Appl. Meteor. Climatol.*, 51, 1145–1163, doi: 10.1175/JAMC-D-11-0203.1, 2012.
- Brisson, E., Van Weverberg, K., Demuzere, M., Devis, A., Saeed, S., Stengel, M., and Van Lipzig, N. P. M.: How well can a convection-permitting climate model reproduce decadal statistics of precipitation, temperature and cloud characteristics?, *Clim. Dyn.*, 47, 3043–3061, doi: 10.1007/s00382-016-3012-z, 2016.
- 10 CM SAF: Algorithm Theoretical Basis Document, SEVIRI cloud products, CLAAS Edition 2, EUMETSAT Satellite Application Facility on Climate Monitoring, SAF/CM/DWD/ATBD/SEV/CLD, Issue 2, Rev. 3, doi: 10.5676/EUM\_SAF\_CM/CLAAS/V002, 17 June 2016, 2016a.
- CM SAF: Algorithm Theoretical Basis Document, SEVIRI Cloud Physical Products, CLAAS Edition 2, EUMETSAT Satellite Application Facility on Climate Monitoring, SAF/CM/KNMI/ATBD/SEVIRI/PPP, Issue 2, Rev. 2, doi: 10.5676/EUM\_SAF\_CM/CLAAS/V002, 10 June 2016, 2016b.
- 15 [de Graaf, M., L. G. Tilstra, P. Wang, and Stammes, P.: Retrieval of the aerosol direct radiative effect over clouds from spaceborne spectrometry, \*J. Geophys. Res.\*, 117, D07207, doi:10.1029/2011JD017160, 2012.](#)
- Dee, D. P., Uppala, S. M., Simmons, A. J., Berrisford, P., Poli, P., Kobayashi, S., Andrae, U., Balmaseda, M. A., Balsamo, G., Bauer, P., Bechtold, P., Beljaars, A. C. M., van de Berg, L., Bidlot, J., Bormann, N., Delsol, C., Dragani, R., Fuentes, M., Geer, A. J., Haimberger, L., Healy, S. B., Hersbach, H., H'olm, E. V., Isaksen, I., Kallberg, P., K'ohler, M., Matricardi, M., McNally, A. P., Monge-Sanz, B. M., Morcrette, J.-J., Park, B.-K., Peubey, C., de Rosnay, P., Tavolato, C., Th'epaut, J.-N., and Vitart, F.: The ERA-Interim reanalysis: configuration and performance of the data assimilation system, *Quart. J. Roy. Meteor. Soc.*, 137, 553–597, 2011.
- 20 Delanoë, J., and Hogan, R. J.: A variational scheme for retrieving ice cloud properties from combined radar, lidar, and infrared radiometer, *J. Geophys. Res.*, 113, D07204, doi:10.1029/2007JD009000, 2008.
- Delanoë, J. and Hogan, R. J.: Combined CloudSat-CALIPSO-MODIS retrievals of the properties of ice clouds, *J. Geophys. Res.*, 115, D00H29, doi:10.1029/2009JD012346, 2010.
- Derrien, M. and Le Gléau, H.: MSG/SEVIRI cloud mask and type from SAFNWC, *Int. J. Remote Sensing*, 26, 4707–4732, 2005.
- 30 Eliasson, S., Holl, G., Buehler, S. A., Kuhn, T., Stengel, M., Iturbide-Sanchez, F., and Johnston, M.: Systematic and random errors between collocated satellite ice water path observations, *J. Geophys. Res. Atm.*, 118, 2629–2642, doi:10.1029/2012JD018381, 2013.
- Haywood, J. M., Osborne, S. R., and Abel, S. J.: The effect of overlying absorbing aerosol layers on remote sensing retrievals of cloud effective radius and cloud optical depth, *Quart. J. Roy. Meteor. Soc.*, 130, 779–800, 2004.

- Heidinger, A. K., Foster, M. J., Walther, A., and Zhao, X.: The Pathfinder Atmospheres Extended (PATMOS-x) AVHRR climate data set, *B. Am. Meteorol. Soc.*, 95, 2014.
- Hess, M., Koelemeijer, R. B. A., and Stammes, P.: Scattering matrices of imperfect hexagonal ice crystals, *J. Quant. Spectrosc. Ra.*, 60(3), 301–308, 1998.
- 5 Jarraud, M.: Guide to Meteorological Instruments and Methods of Observation (WMO - No.8), World Meteorological Organisation, Geneva, Switzerland, 2008.
- Karlsson, K.-G.: A ten-year cloud climatology over Scandinavia derived from NOAA AVHRR imagery, *Int. J. Climatol.*, 23, 1023-1044, doi:10.1002/joc.916, 2003.
- Karlsson, K.-G., Riihelä, A., Müller, R., Meirink, J. F., Sedlar, J., Stengel, M., Lockhoff, M., Trentmann, J., Kaspar, F.,  
10 Hollmann, R., and Wolters, E.: CLARA-A1: a cloud, albedo, and radiation dataset from 28 yr of global AVHRR data, *Atmos. Chem. Phys.*, 13, 5351–5367, doi:10.5194/acp-13-5351-2013, 2013.
- Karlsson, K.-G., Anttila, K., Trentmann, J., Stengel, M., Meirink, J. F., Devasthale, A., Hanschmann, T., Kothe, S., Jääskeläinen, E., Sedlar, J., Benas, N., van Zadelhoff, G.-J., Schlundt, C., Stein, D., Finkensieper, S., Håkansson, N. and Hollmann, R.: CLARA-A2: The second edition of the CM SAF cloud and radiation dataset record from 34 years of global  
15 AVHRR data, *Atmos. Chem. Phys. Discuss.*, doi:10.5194/acp-2016-935, in review, 2016.
- [Knap, W. H., Labonnote, L. C., Brogniez, G., and Stammes, P.: Modeling total and polarized reflectances of ice clouds: evaluation by means of POLDER and ATSR-2 measurements. \*Appl. Optics\*, 44, 4060-4073, 2005.](#)
- Maddux, B. C., Ackerman, S. A., and Platnick, S.: Viewing Geometry Dependencies in MODIS Cloud Products, *J. Atm. Ocean. Tech.*, 27(9), 1519-1528, doi: 10.1175/2010JTECHA1432.1, 2010.
- 20 Martins, J. P. A., Cardoso, R. M., Soares, P. M. M., Trigo, I. F., Belo-Pereira, M., Moreira, N., and Tomé, R.: The summer diurnal cycle of coastal cloudiness over west Iberia using Meteosat/SEVIRI and a WRF regional climate model simulation, *Int. J. Climatol.*, 36, 1755–1772, doi:10.1002/joc.4457, 2016.
- Matricardi, M., Chevallier, F., Kelly, G., and Thepaut, J.-N.: An improved general fast radiative transfer model for the assimilation of radiance observations, *Quart. J. Roy. Meteor. Soc.*, 130, 153–173, doi: 10.1256/qj.02.181, 2004.
- 25 Meirink, J. F., Roebeling, R. A., and Stammes, P.: Inter-calibration of polar imager solar channels using SEVIRI, *Atmos. Meas. Tech.*, 6, 2495–2508, doi: 10.5194/amt-6-2495-2013, 2013.
- Menzel, W. P., Smith, W. L., and Stewart, T. R.: Improved Cloud Motion Wind Vector and Altitude Assignment using VAS, *J. Appl. Meteorol. Clim.*, 22, 377–384, 1983.
- Moody, E. G., King, M. D., Platnick, S., Schaaf, C. B., and Gao, F.: Spatially complete global spectral surface albedos: value-added datasets derived from Terra MODIS land products, *IEEE T. Geosci. Remote S.*, 43, 144–158, 2005.
- 30 Nakajima, T. and King, M. D.: Determination of the optical thickness and effective particle radius of clouds from reflected solar radiation measurements, part 1: Theory, *J. Atmos. Sci.*, 47, 1878–1893, 1990.

- NWC SAF: Scientific report on improving “Cloud Products” (CMA-PGE01 v3.1, CT-PGE02 v2.1 & CTTH-PGE03 v2.2), EUMETSAT Satellite Application Facility on Nowcasting and Short range Forecasting, SAF/NWC/CDOP/MFL/SCI/RP/06, Issue 1, Rev. 0, 24 March 2011, 2011.
- NWC SAF: Algorithm Theoretical Basis Document for “Cloud Products” (CMA-PGE01 v3.2, CT-PGE02 v2.2 and CTTH-PGE03 v2.2), EUMETSAT Satellite Application Facility on Nowcasting and Short range Forecasting, SAF/NWC/CDOP2/MFL/SCI/ATBD/01, Issue 3, Rev. 2.1, 15 July 2013, 2013.
- O’Dell, C. W., Wentz, F. J., and Bennartz, R.: Cloud liquid water path from satellite-based passive microwave observations: a new climatology over the global oceans, *J. Climate*, 21, 1721–1739, 2008.
- OSI SAF: The EUMETSAT OSI SAF Sea Ice Concentration Algorithm. Algorithm Theoretical Basis Document, SAF/OSI/CDOP/DMI/SCI/MA/189, Version 1.5, 2016.
- Pavolonis, M. J., Heidinger, A. K., and Uttal, T.: Daytime global cloud typing from AVHRR and VIIRS: Algorithm description, validation, and comparison, *J. Appl. Meteorol.*, 44, 804–826, doi:10.1175/JAM2236.1, 2005.
- Pfeifroth, U., Trentmann, J., Fink, A., and Ahrens, B.: Evaluating Satellite-Based Diurnal Cycles of Precipitation in the African Tropics, *J. Appl. Meteor. Climatol.*, 55, 23–39, doi: 10.1175/JAMC-D-15-0065.1, 2016.
- Platnick, S. E., King, M. D., Ackerman, S. A., Menzel, W. P., Baum, B. A., Riédi, J. C., and Frey, R. A.: The MODIS cloud products: Algorithms and examples from Terra, *IEEE T. Geosci. Remote S.*, 41, 459–473, 2003.
- Platnick, S., King, M. D., Meyer, K. G., Wind, G., Amarasinghe, N., Marchant, B., Arnold, G. T., Zhang, Z., Hubanks, P. A., Ridgway, B., and Riédi, J.: MODIS Cloud Optical Properties: User Guide for the Collection 6 Level-2 MOD06/MYD06 Product and Associated Level-3 Datasets, Version 1.0, available at [http://modis-atmos.gsfc.nasa.gov/\\_docs/C6MOD06OPUserGuide.pdf](http://modis-atmos.gsfc.nasa.gov/_docs/C6MOD06OPUserGuide.pdf), last access: 31 May 2016, 2015
- Reuter, M., Thomas, W., Albert, P., Lockhoff, M., Weber, R., Karlsson, K.-G., and Fischer, J.: The CM-SAF and FUB Cloud Detection Schemes for SEVIRI: Validation with Synoptic Data and Initial Comparison with MODIS and CALIPSO, *J. Appl. Meteorol. Climatol.*, 48, 301–316, doi:10.1175/2008JAMC1982.1, 2009.
- Roebeling, R. A., Feijt, A. J., and Stammes, P.: Cloud property retrievals for climate monitoring: implications of differences between SEVIRI on METEOSAT-8 and AVHRR on NOAA-17, *J. Geophys. Res.*, 111, D20 210, 2006.
- Rossow, W. B. and Schiffer, R. A.: Advances in understanding clouds from ISCCP, *B. Am. Meteorol. Soc.*, 80, 2261–2287, 1999.
- Salomonson, V. V., Barnes, W. L., Maymon, P. W., Montgomery, H. E., and Ostrow, H.: MODIS: Advanced facility instrument for studies of the earth as a system, *IEEE Trans. Geosci. Remote Sens.*, 27, 145–153, doi:10.1109/36.20292, 1989.
- Saunders, R., Matricardi, M., and Brunel, P.: An improved fast radiative transfer model for assimilation of satellite radiance observations, *Q. J. Roy. Meteor. Soc.*, 125, 1407–1425, doi: 10.1002/qj.1999.49712555615, 1999.
- Schmetz, J., Holmlund, K., Hoffman, J. and Strauss, B., Mason, B., Gaertner, V., Koch, A., and Van De Berg, L.: Operational cloud motion winds from Meteosat infrared images, *J. Appl. Meteorol.*, 32, 7, 1206–1225, 1993.

- Schulz, J., Albert, P., Behr, H.-D., Caprion, D., Deneke, H., Dewitte, S., D'urr, B., Fuchs, P., Gratzki, A., Hechler, P., Hollmann, R., Johnston, S., Karlsson, K.-G., Manninen, T., Müller, R., Reuter, M., Riihelä, A., Roebeling, R., Selbach, N., Tetzlaff, A., Thomas, W., Werscheck, M., Wolters, E., and Zelenka, A.: Operational climate monitoring from space: the EUMETSAT Satellite Application Facility on Climate Monitoring (CM-SAF), *Atmos. Chem. Phys.*, 9, 1687–1709, 2009.
- 5 Segelstein, D.: The complex refractive index of water, M.Sc. Thesis, University of Missouri, Kansas City, 1981.
- Stammes, P.: Spectral radiance modelling in the UV-Visible range, in: *IRS 2000: Current problems in Atmospheric Radiation*, edited by Smith, W. L. and Timofeyev, Y. M., pp. 385–388, A. Deepak, Hampton, VA, 2001.
- Stengel, M. S., Kniffka, A. K., Meirink, J. F. M., Lockhoff, M. L., Tan, J. T., and Hollmann, R. H.: CLAAS: the CM SAF cloud property data set using SEVIRI, *Atmos. Chem. Phys.*, 14, 4297–4311, doi:10.5194/acp-14-4297-2014, 2014.
- 10 Stephens, G.: Radiation profiles in extended water clouds, II: Parameterization schemes, *J. Atmos. Sci.*, 35, 2123–2132, 1978.
- Stocker, T. F., Qin, D., Plattner, G.-K., Tignor, M., Allen, S. K., Boschung, J., Nauels, A., Xia, Y., Bex, V., and Midgley, P., eds.: *Climate Change 2013: The physical science basis. Contribution of Working Group I to the Fifth Assessment Report of the Intergovernmental Panel on Climate Change*, Cambridge University Press, Cambridge, United Kingdom and New York, NY, USA, 2013.
- 15 [Sun, W., Videen, G., Kato, S., Lin, B., Lukashin, C., and Hu, Y.: A study of subvisual clouds and their radiation effect with a synergy of CERES, MODIS, CALIPSO and AIRS data, \*J. Geophys. Res.\*, 116, D22207, doi:10.1029/2011JD016422, 2011.](#)  
[Tilstra, L. G., de Graaf, M., Aben, I., and Stammes, P.: In-flight degradation correction of SCIAMACHY UV reflectances and Absorbing Aerosol Index, \*J. Geophys. Res.\*, 117, D06209, doi:10.1029/2011JD016957, 2012.](#)
- 20 Warren, S. G., and Brandt, R. E.: Optical constants of ice from the ultraviolet to the microwave: A revised compilation, *J. Geophys. Res.*, 113, D14220, doi:10.1029/2007JD009744, 2008.
- Winker, D. M., Vaughan, M. A., Omar, A., Hu, Y., Powell, K. A., Liu, Z., Hunt, W. H., and Young, S. A.: Overview of the CALIPSO Mission and CALIOP data processing algorithms, *J. Atmos. Oceanic Technol.*, 26, 2310–2323, doi:10.1175/2009JTECHA1281.1, 2009.
- 25 Wu, A., Xiong, X., Doelling, D. R., Morstad, D., Angal, A., and Bhatt, R.: Characterization of Terra and Aqua MODIS VIS, NIR, and SWIR spectral bands' calibration stability, *IEEE T. Geosci. Remote S.*, 51, 4330–4338, 2013.
- Yang, P., Bi, L., Baum, B. A., Liou, K. N., Kattawar, G. W., Mishchenko, M. I., and Cole, B.: Spectrally consistent scattering, absorption, and polarization properties of atmospheric ice crystals at wavelengths from 0.2 to 100  $\mu\text{m}$ , *J. Atmos. Sci.*, 70, 330–347, doi: 10.1175/JAS-D-12-039.1, 2013.



**Table 1: Specification of the LUTs created with DAK: for all variables spanning the axes of the LUTs their discrete values are given.**

Variable	Range	Number of points
cos(SZA)	0.099 – 1 (SZA: 0 – 84.3°)	73, Gauss points
cos(VZA)	same as cos(SZA)	same as cos(SZA)
Relative Azimuth Angle	0 - 180°	91, equidistant
COT	0 and 0.25 – 256	22, equidistant in log(COT)
REF liquid <sup>a</sup>	3 – 34 μm	8, equidistant in log(REF)
REF ice <sup>b</sup>	5 – 80 μm	9, equidistant in log(REF)

<sup>a</sup> Single scattering properties have been calculated using Mie theory for spherical droplets with a two-parameter gamma size distribution (effective variance = 0.15) and complex refractive index from Segelstein (1981).

<sup>b</sup> Single scattering properties have been calculated using ray tracing for [randomly oriented](#) monodisperse imperfect hexagonal ice crystals (Hess et al., 1998) with aspect ratios from Yang et al. (2013), roughening simulated with a distortion angle of 30°, and complex refractive index from Warren and Brandt (2008). [The choice of this ice particle model is motivated by Knap et al. \(2005\) who showed that it yields adequate simulations of total and polarized ice cloud reflectances observed by the Polarization and Directionality of Earth Reflectances \(POLDER\) instrument.](#)

**Table 2: Contingency table for the CLAAS-2 and CALIOP observations.  $n$  is the number of cases, 1 and 2 correspond to clear/cloudy for the cloud mask and water/ice for the cloud phase.**

	CALIOP reports 1	CALIOP reports 2
CLAAS-2 reports 1	$n_{11}$	$n_{12}$
CLAAS-2 reports 2	$n_{21}$	$n_{22}$

5

10

15

20

25

30

**Table 3: Validation results for CLAAS-2 level 2 cloud mask (CMa) and cloud phase (CPH).**

		CALIOP ICOT > 0.0					CALIOP ICOT > 0.2				
		All	Day	Night	Sea	Land	All	Day	Night	Sea	Land
CMa	POD clear	69.4	67.1	71.9	58.0	88.0	61.4	58.3	64.9	49.6	80.6
	FAR clear	23.6	20.7	26.4	18.6	28.2	5.5	3.4	7.5	2.9	7.9
	POD cloudy	87.5	88.7	86.5	93.1	75.2	96.2	97.5	95.2	98.6	90.3
	FAR cloudy	16.9	19.3	14.6	19.1	10.2	29.8	34.3	25.3	31.9	23.1
	Hitrates	80.9	80.3	81.5	81.1	80.6	78.3	75.9	80.7	75.1	84.6
	KSS	56.9	55.9	58.4	51.1	63.2	57.6	55.8	60.1	48.3	70.9
CPH	POD liquid	91.6	89.3	93.7	92.9	84.7	85.5	83.7	87.0	88.0	74.8
	FAR liquid	29.8	27.3	31.9	25.2	48.2	10.0	9.8	10.2	7.6	20.1
	POD ice	74.9	77.9	72.3	73.6	77.3	88.9	90.1	87.7	89.1	88.4
	FAR ice	6.7	8.3	5.2	7.5	5.4	16.0	16.4	15.6	16.7	14.9
	Hitrates	81.4	82.4	80.6	82.4	79.0	87.0	86.8	87.3	88.5	83.2
	KSS	66.5	67.2	66.0	66.5	62.0	74.4	73.8	74.7	77.2	63.2

5

10

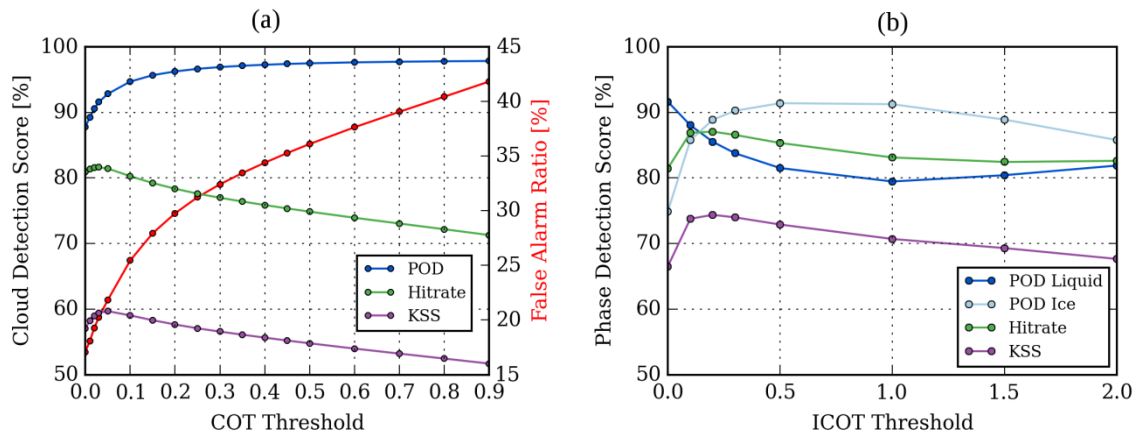


**Figure 1: (a) CLAAS-2 cloud detection scores as a function of the COT threshold used to discriminate clear and cloudy CALIOP observations. KSS denotes the Hanssen-Kuiper skill score. (b) CLAAS-2 cloud phase detection scores as a function of the integrated COT (ICOT) threshold, which determines the reference cloud layer.**

5

10

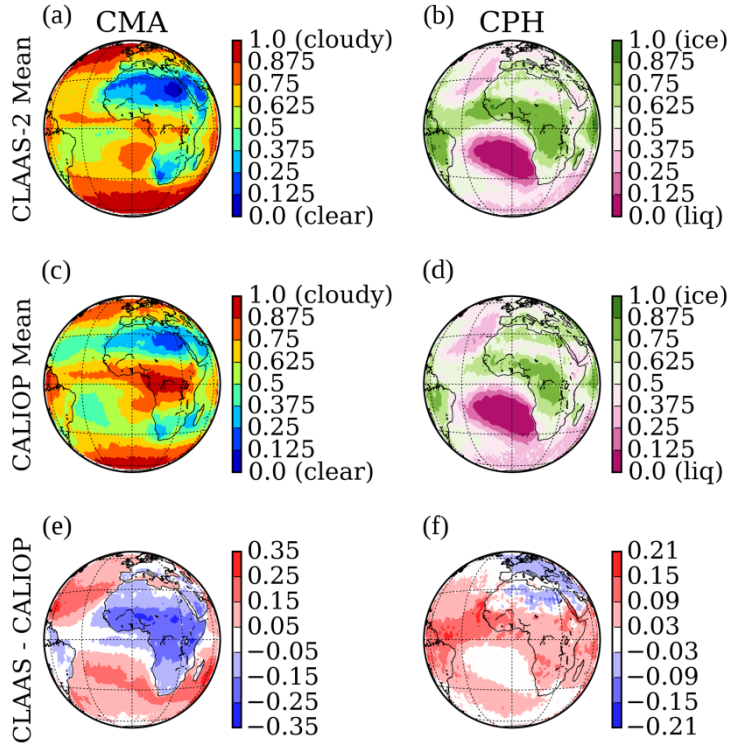


**Figure 2: Spatial distribution of cloud fraction from CLAAS-2 level 2 (a) and CALIOP (c), as well as fraction of ice clouds (b and d, respectively). The bottom row shows the absolute difference CLAAS-CALIOP for cloud fraction (e) and fraction of ice clouds (f). Note the different scaling in (e) and (f). CALIOP cloud detection criterion is total column COT>0, while CALIOP phase is taken from the layer where ICOT exceeds 0.2.**

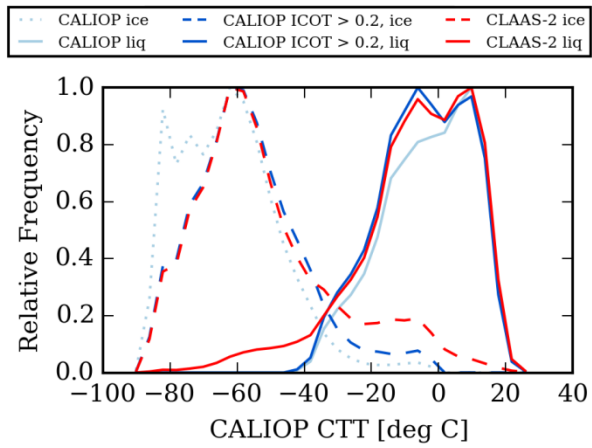


**Figure 3:** Phase histograms for liquid and ice clouds as a function of CALIOP cloud top temperature. For the red and blue lines, binning is based on the CALIOP CTT taken from the layer where ICOT exceeds 0.2. For the light-blue line, phase and temperature of the uppermost CALIOP cloud layer were used. Bin size is 4 °C.

5

10

15

20

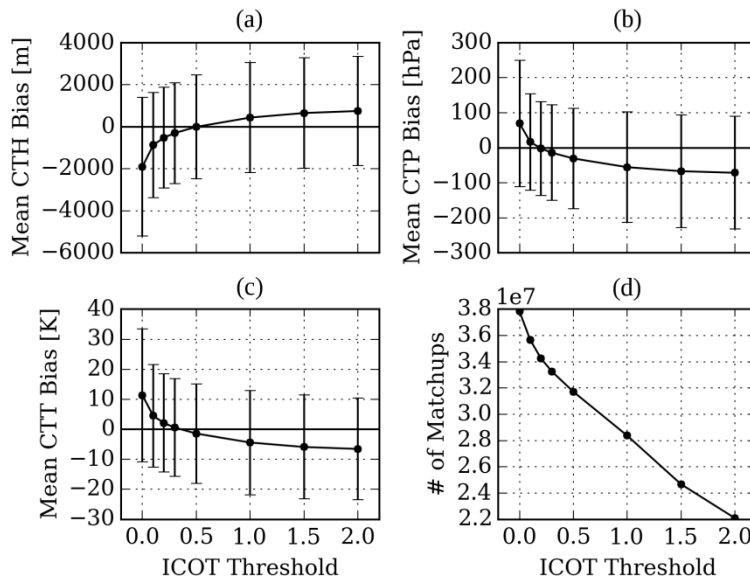


**Figure 4: Mean biases (CLAAS-2 – CALIOP) of CTH (a), CTP (b) and CTT (c), compared against the CALIOP cloud layer where ICOT exceeds a certain threshold. Error bars represent the bc-RMSE. The number of collocated measurements is also shown (d).**

5

10

15

20

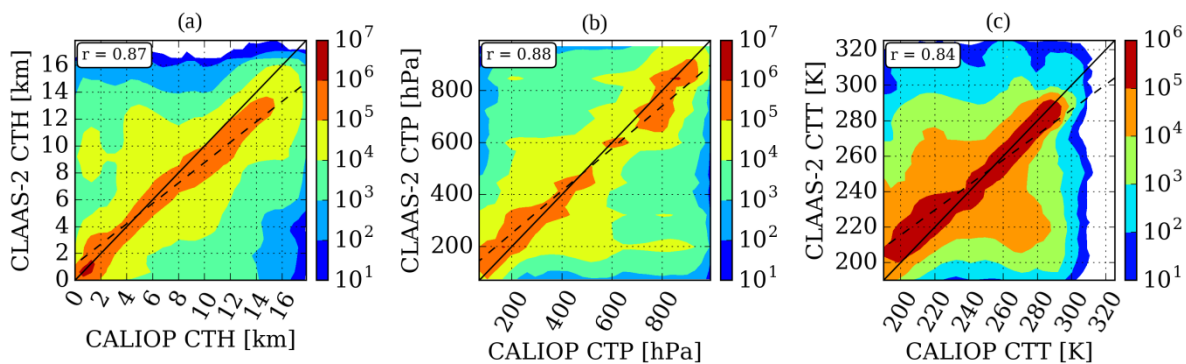


**Figure 5: Scatter plots of cloud top products between CLAAS-2 and CALIOP: CTH (a), CTP (b) and CTT (c). The diagonal is marked by a solid line; dashed lines show the result of a least squares linear fit. The textbox in the upper left corner displays the Pearson correlation coefficient. p-values are practically zero because of the very large number of matchups. CALIOP values were**



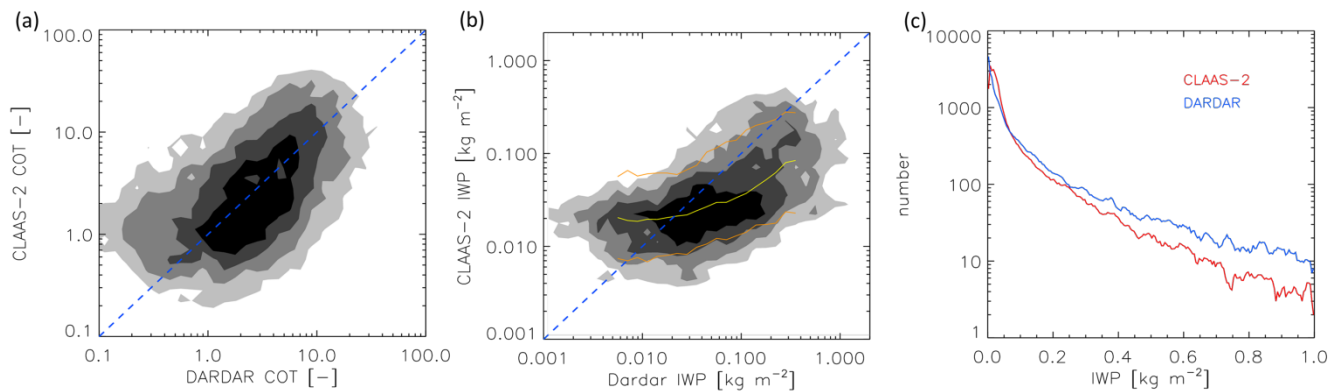


**Figure 6: (a) Ice COT distribution comparing the DARDAR and CLAAS-2 retrieved collocated values. The blue dashed line shows the 1:1 line and the grey scales indicate the regions enclosing 20, 40, 60 and 75% of all data points. (b) As in (a), for the IWP. The yellow line depicts the median and the orange the 16<sup>th</sup>/84<sup>th</sup> percentiles of the CLAAS-2 distribution at the corresponding DARDAR IWP. (c) 1-D histogram of DARDAR and CLAAS-2 IWP for the same collocations.**

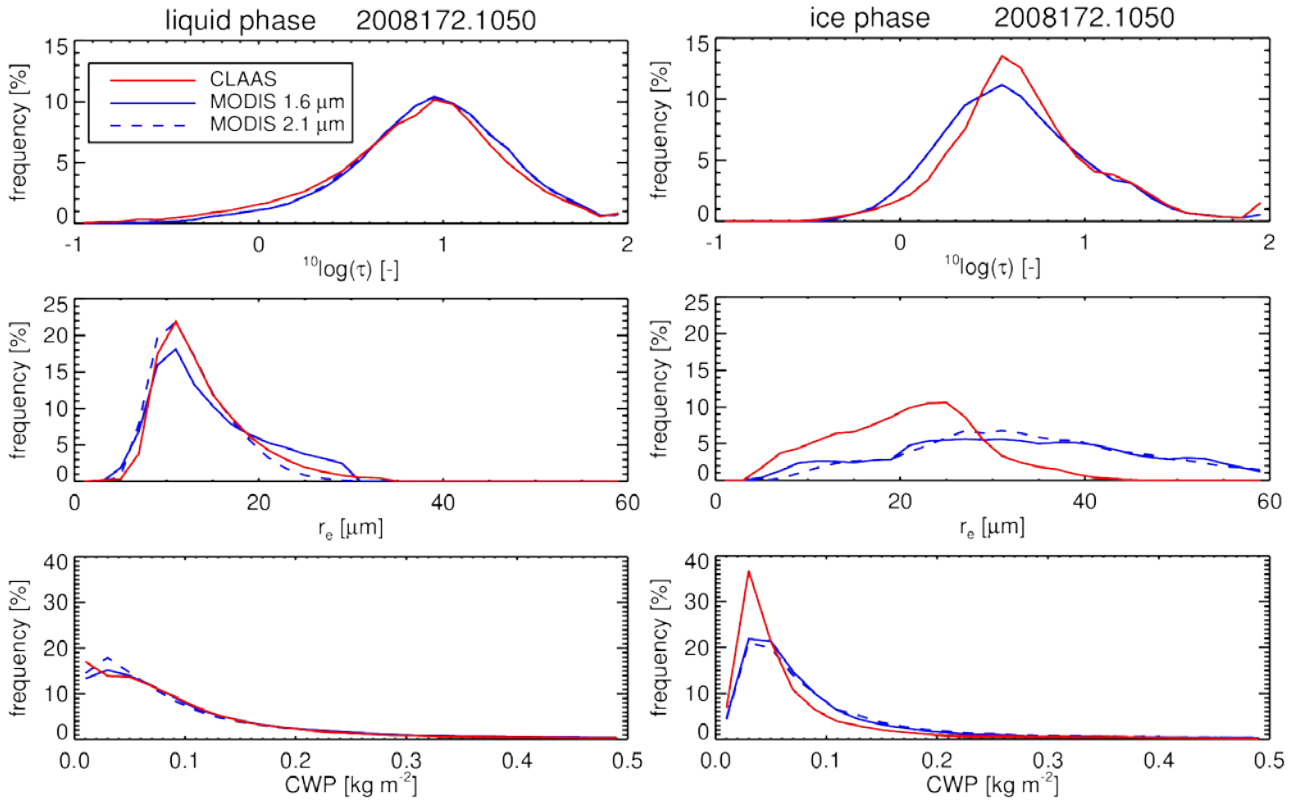


**Figure 7: Histograms of CLAAS-2 and MODIS COT (top), REF (middle), and CWP (bottom) for the selected MODIS granule on 20 June 2008. Left: liquid clouds; right: ice clouds. Only pixels for which both products agree on CPH are included. For MODIS the standard and PCL (partly cloudy) retrievals were combined, and results are shown for retrievals with two different wavelength bands (1.6 and 2.1  $\mu\text{m}$ ). Note that differences between MODIS 1.6 and 2.1  $\mu\text{m}$  based COT are small. Hence, the solid and dashed blue lines in the top panels cannot be distinguished. Only pixels for which both products agree on CPH are included.**

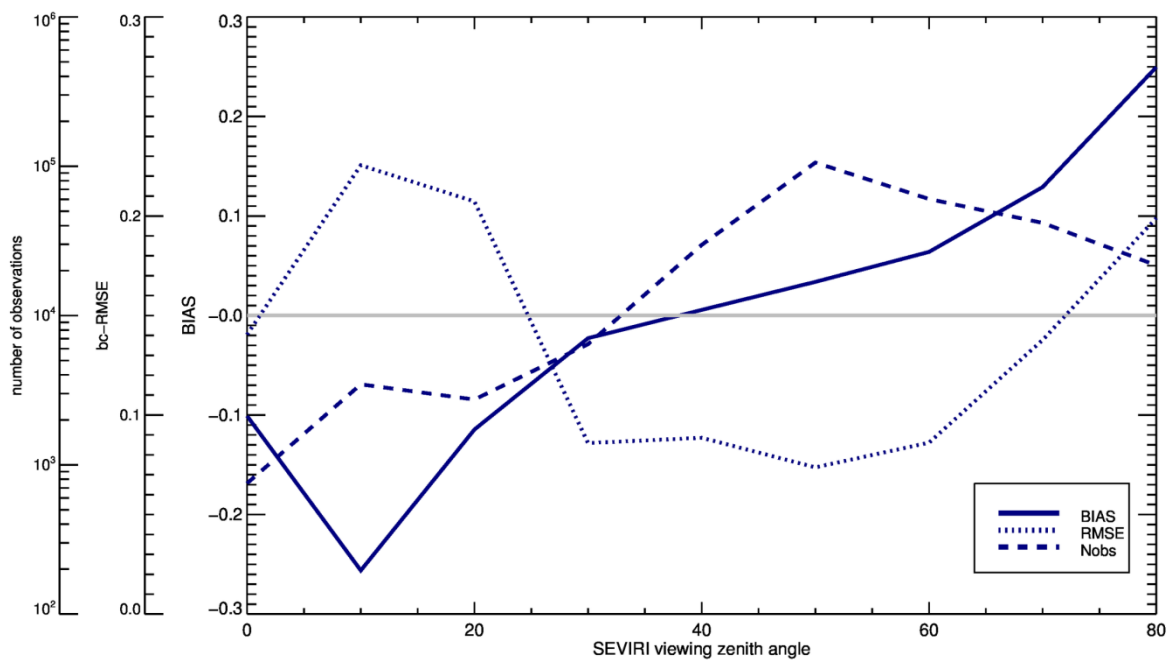


**Figure 8: Dependency of the level 3 CLAAS-2 – SYNOP CFC bias, bc-RMSE and SYNOP number of observations on SEVIRI viewing zenith angle.**

5

10

15

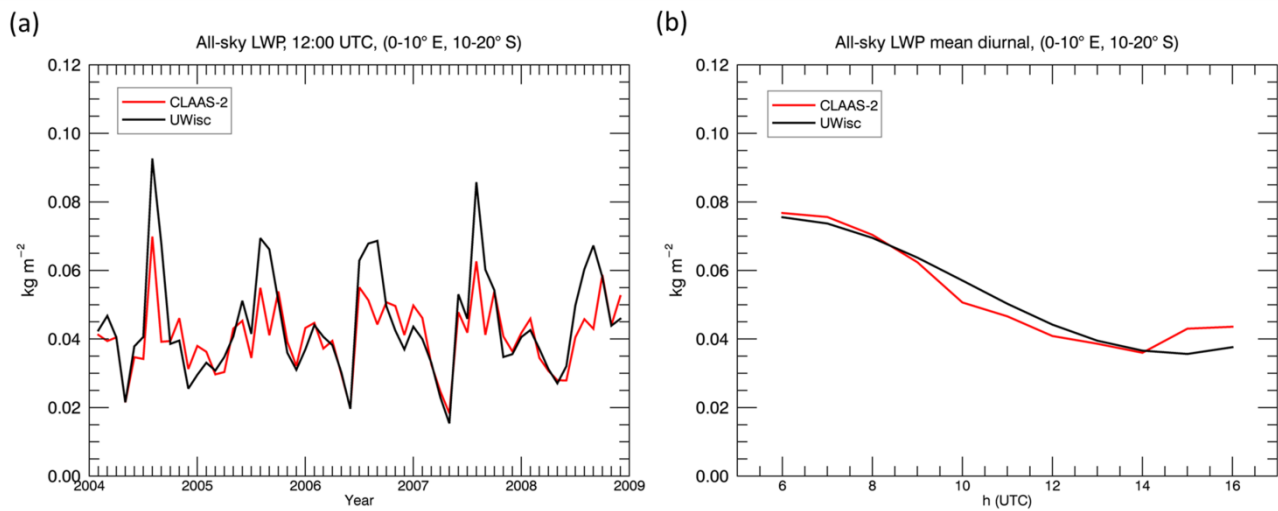


**Figure 9: (a) Time series of the monthly all-sky LWP over the marine Sc region (0-10° E, 10-20° S) at 12:00 UTC from CLAAS-2 and UWisc data. (b) Monthly mean diurnal cycle of all-sky LWP from CLAAS-2 and UWisc over the same region.**

5

10

15

20

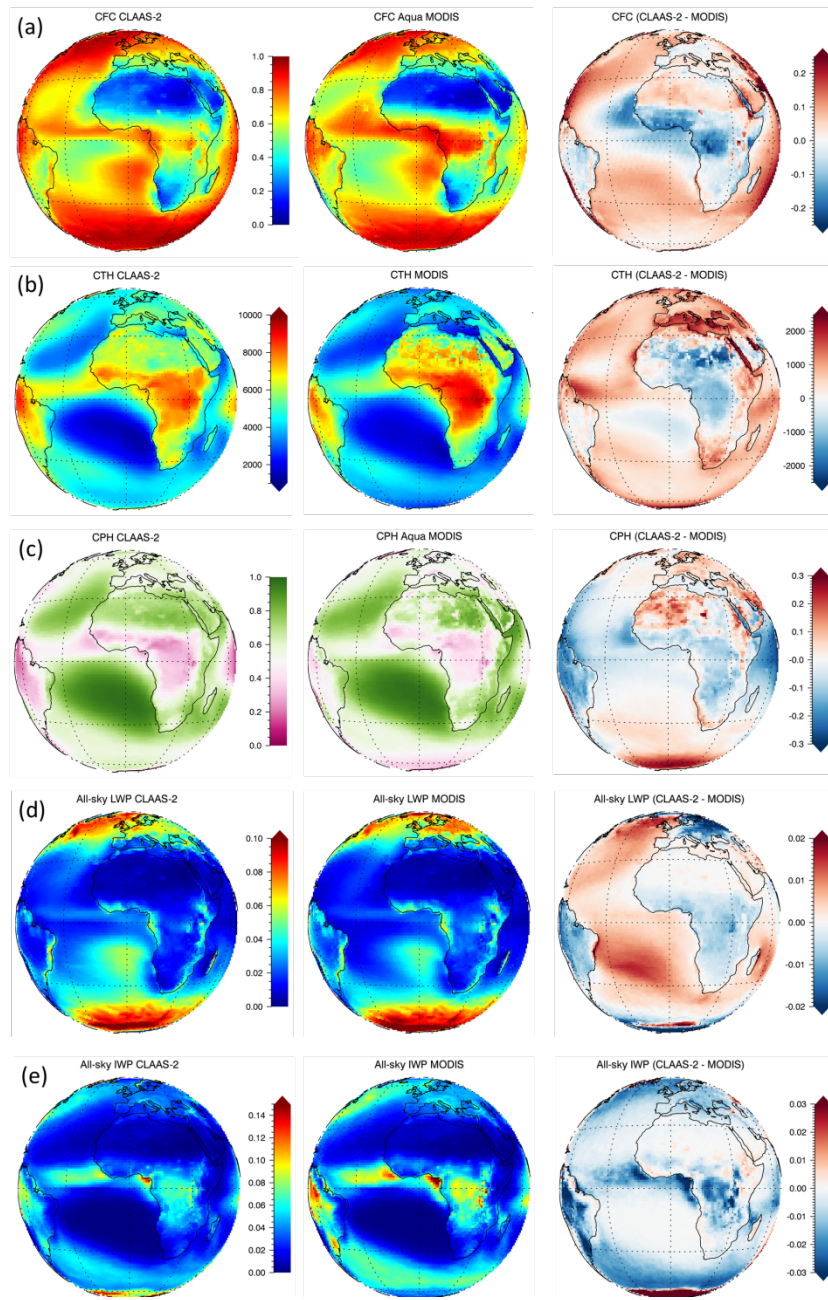
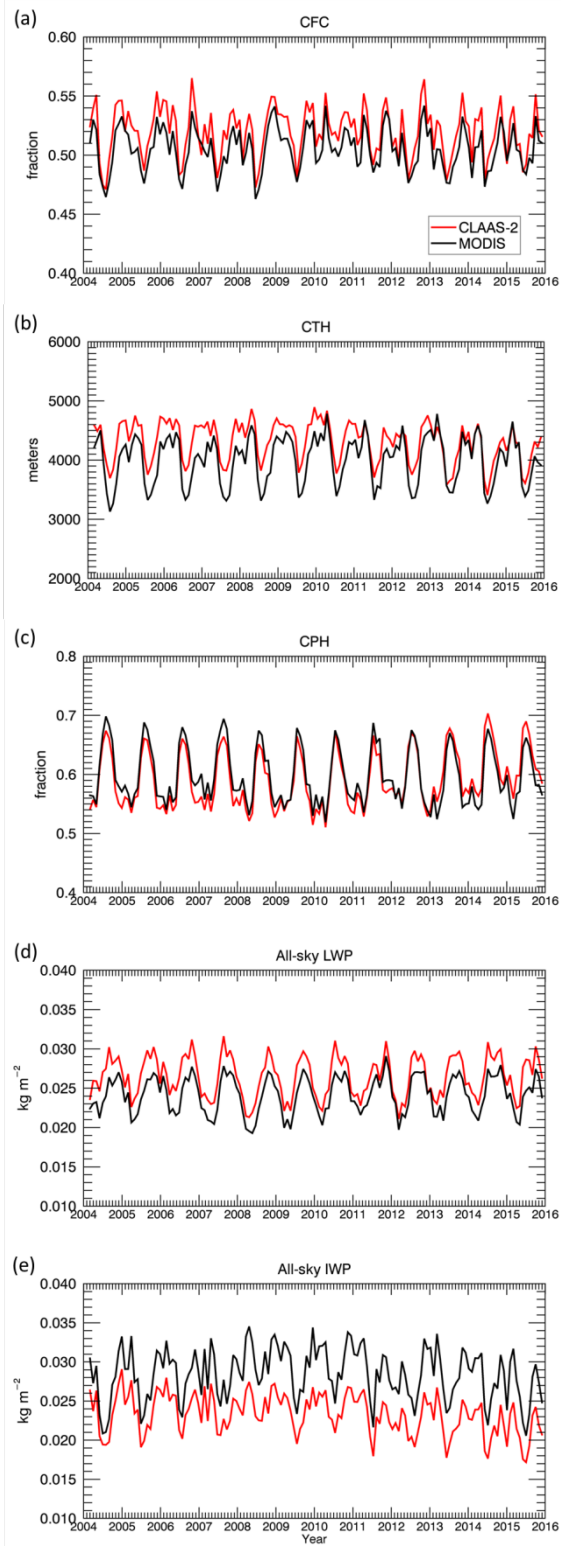


Figure 10: Spatial distributions of CFC (a), CTH (b), CPH (liquid cloud fraction) (c), all-sky LWP (d) and all-sky IWP (e), averaged from February 2004 until December 2015 from CLAAS-2 (left column) and MODIS (middle column). The right column shows corresponding differences. Aqua MODIS data were used in (a) and (c); average Aqua and Terra MODIS data were used in (b), (d) and (e). Units are fraction (a, c), meters (b) and  $\text{kg m}^{-2}$  (d, e).



**Figure 11: Time series of the 45° W-E and S-N area-averaged CFC (a), CTH (b), CPH (liquid cloud fraction) (c), all-sky LWP (d) and all-sky IWP (e) from CLAAS-2 and MODIS. Aqua MODIS data were used in (a) and (c); average Aqua and Terra MODIS data were used in (b), (d) and (e).**